MECHANISM OF INTERANNUAL CROSS-EQUATORIAL OVERTURNING ANOMALIES IN THE PACIFIC OCEAN

DEVANARAYANA RAO MOHAN RAO

A THESIS SUBMITTED TO
THE FACULTY OF GRADUATE STUDIES
IN PARTIAL FULFILLMENT OF THE REQUIREMENTS
FOR THE DEGREE OF

MASTER OF SCIENCE

GRADUATE PROGRAM IN EARTH AND SPACE SCIENCE
YORK UNIVERSITY
TORONTO, ONTARIO

DECEMBER 2020

Abstract

Recent evidence shows that the variability of meridional overturning circulation (MOC) in the Indian and Pacific Oceans (PMOC) is characterized by a prominent cross-equatorial cell (CEC) spanning the tropics between 20°S and 20°N, but the mechanism responsible for this CEC is not understood. Using version 4.2 of the Estimating the Circulation and Climate of the Ocean (ECCO) state estimate, our investigation shows the mechanism responsible for CEC can be conceptualized by following mechanistic chain: 1) Anomalous winds produce equatorially antisymmetric anomalies of zonal mean sea surface temperature (SST) in the Pacific Ocean, 2) These temperature anomalies generate equatorially antisymmetric anomalies of sea surface height (SSH), 3) The SSH anomalies generate a cross-equatorial flow in the upper Pacific Ocean (above approximately 1000 m), and 4) This anomalous cross-equatorial flow in the upper layers drives compensating circulation in the deep Pacific.

Acknowledgements

Any accomplishment will never be a success without God's grace and it is no different in this project. I thank the Almighty for guiding me through this project and lending me His assistance in different forms whenever I have met with difficulties.

I am very happy to present this project, "Mechanism of Interannual Cross-equatorial Overturning Anomalies in the Pacific Ocean", which I undertook as a part of my graduate program in Earth and Space Science at York University, Toronto from January 2019 to December 2020. Apart from my efforts, the success of my project depends largely on the encouragement and guidance of many others. I take this opportunity to express my gratitude to all people who have been instrumental in the successful completion of the project.

Firstly, I am highly indebted to my guide Dr. Neil F.Tandon, for his valuable and timely instructions, whole-hearted support, and constant encouragement, which brought out the best in me.

I take this opportunity to acknowledge my sincere thanks to Dr. Peter Taylor, the supervisory committee member, for the feedback and advice given to me during this project.

I would like to express my sincere thanks to Dr. Kaz Higuchi and Dr. Gary Klaassen, for their feeback given to me during the oral examination.

I acknowledge, with profound gratitude, the patronage extended to me by York University and the Faculty of Graduate Studies for the financial assistance. I would like to express my deepest thanks to Dr. Mark Gordon, Graduate Program Director, Dept.of Earth and Space Science and Engineering (ESSE), and Marcia Gaynor, Graduate Program Assistant of ESSE for their support and assistance. I would like to express my sincere thanks to Dr. Kathy L.Young for her valuable lessons in the dynamics of snow and ice.

I express my heartfelt thanks to Dr. Shanoja Naik, Noah Stanton, Thabo Mpanza, Christian B. Schuler, Alex M. J., and Harikrishna Rao for the facilities they had extended to me and their personal support. I thank the course directors and my colleagues for their support during my teaching assistantship.

Last but not the least, I would like to thank my family, and friends at N.I.O.,Goa and C.U.S.A.T. for their constant support and encouragement.

Devanarayana Rao Mohan Rao

Dedication

To my mentor, teachers, friends and family,
I couldn't have done this without you.

Table of Contents

List of Figures

List of Acronyms

AABW	Antarctic Bottom Water
AMOC	Atlantic MOC
BoB	Bay of Bengal
CanESM2	Canadian Earth System Model vesrion 2
CEC	Cross-equatorial Cell
ECCO	Estimating the Circulation and Climate of the Ocean
ENSO	El Niño Southern Oscillation
EOF	Empirical Orthogonal Function
EUC	Equatorial Undercurrent
IOD	Indian Ocean Dipole
IPCC	Intergovernmental Panel on Climate Change
ISTD	Interannual Standard Deviation
ITF	Indonesian Through Flow
MHT	Meridional Heat Transport
MOC	Meridional Overturning Circulation
NADW	North Atlantic Deep Water
NEC	North Equatorial Current
NECC	North Equatorial Counter Current
NH	Northern Hemisphere
OGCM	Ocean General Circulation Model
PC	Principal Component
PCA	Principal Component Analysis
PMOC	Indo-Pacific MOC
SEC	South Equatorial Current
SH	Southern Hemisphere
SODA	Simple Ocean Data Assimilation
SSH	Sea Surface Height
SSI	SSH Seesaw Index
SSI	Sea Surface Temperature
ZWS	Zonal Wind Stress

List of Mathematical Symbols

Ψ	MOC Streamfunction (Sv)
x	Longitude Axis (degrees)
y	Latitude Axis (degrees)
z	Depth (m)
u	Current Velocity in x-direction $(\mathrm{m\ s^{-1}})$
v	Current Velocity in y-direction $(\mathrm{m\ s^{-1}})$
w	Current Velocity in z-direction $(\mathrm{m\ s^{-1}})$
w_E	Ekman Pumping velocity $(\mathrm{m\ s^{-1}})$
S	Salinity of Seawater $(\mathrm{g\ kg^{-1}})$
T	Temperature of Seawater (°C)
ρ	Density of Seawater $(\mathrm{kg\ m^{-3}})$
θ	Potential Temperature (°C)
σ_t	Sigma-t $(\mathrm{kg\ m^{-3}})$
p	Pressure of Seawater (dbar)
η	Sea Surface Height (m)
D	Dynamic Height $(\mathrm{m^2\ s^{-2}})$
Φ	Geopotential Height $(\mathrm{m^2\ s^{-1}})$
δ	Specific Volume Anomaly $(\mathrm{m^3\ kg^{-1}})$
τ	Surface Wind Stress $(\mathrm{N\ m^{-2}})$
f	Coriolis Parameter $(\mathrm{rad\ s^{-1}})$
ω	Angular Velocity of Earth $(\mathrm{rad\ s^{-1}})$
φ	Latitude (degrees)
A_z	Vertical Eddy Viscosity $(\mathrm{m^2\ s^{-1}})$
κ	Bulk Modulus $(\mathrm{N\ m^{-2}})$
α	Coefficient of Thermal Expansion $(°\mathrm{C}^{-1})$
β	Coefficient of Saline Contraction
ψ	Eigenvector
λ	Eigenvalue
S	Covariance Matrix
X	Data Matrix
m	Grid Points in Space
n	Grid Points in Time

Chapter 1

INTRODUCTION

Oceanography is the scientific study of the ocean with branches in biological, geological, physical, and chemical sciences. Physical oceanography describes the evolving patterns of ocean circulations and distribution of properties. In particular, it deals with physical processes in the ocean over a broad range of temporal and spatial scales. In general, the dynamics of the physical processes are studied on scales that range from hundreds of metres to thousands of kilometres in space and timescales of hours to thousands of years [Talley et al., 2011]. Figure 1.1 is an infographic that represents different physical processes based on temporal and spatial scales. In Figure 1.1, the bubbles are microscopic turbulent processes

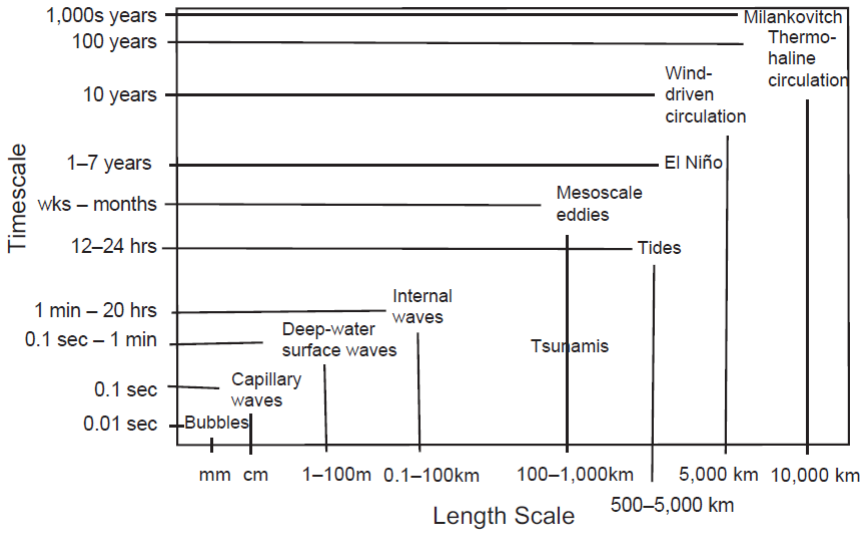

Figure 1.1: The time and spatial scales of oceanographic processes. Reprinted from Talley et al. [2011].

with timescales of milliseconds and spatial scales of a few millimetres. Mesoscale eddies, tides, tsunamis, thermohaline circulation, and Milankovitch cycles (glacial changes) manifest at larger spatial and temporal scales. Microscopic processes such as sea spray, bubbles, and capillary waves have significant impacts on air-sea interactions as well as on sediments that are transported in the coastal zones. In general, Figure 1.1 can be summarized in two different ways : (1) the shorter the timescale, the shorter the spatial scale, and (2) longer

timescale processes are associated with longer spatial scales. These oceanic processes have important implications for climate while interacting with the atmosphere, cryosphere, and lithosphere.

1.1 Ocean Circulation

The ocean circulation refers to the movement of seawater related to variations in different layers of the ocean [Talley et al., 2011, Pond and Pickard, 1983]. These variations are mainly due to changes in the physical properties of sea water (such as temperature and salinity) as well as changes in atmospheric conditions. Thus, the ocean circulation can be conceptualized into two components: (1) surface current systems and (2) deep thermohaline circulation. The near-surface currents transport water on timescales of a few months while the thermohaline circulation takes more than a hundred years to transport water.

1.1.1 Surface Current Systems

The surface current is a continuous movement of water in a particular direction. Different patterns of the surface currents are determined by the wind direction which are visible from satellite measurements as well as in-situ observations. Only horizontal currents are observable, and the vertical currents are weaker than horizontal currents. These circulations have a direct impact on navigation, biological productivity, and the dispersion of chemical constituents. The magnitude of ocean currents can range from centimetres per second (cm s^{-1}) to metres per second (m s^{-1}). The Gulf stream and Antarctic circumpolar currents are relatively fast ocean currents with velocities of nearly 9 kilometres per hour (km hr^{-1}) and 4 km hr^{-1} respectively. These surface currents transport millions of cubic metres of water per second [Talley et al., 2011, Pond and Pickard, 1983]. The oceanographic unit for volumetric rate of transport of ocean current is Sverdrup (Sv), equvivalent to one million cubic metres per second.

Figure 1.2 shows the mean global surface currents. The characteristics of the surface circulation depend on the size and shape of the ocean basin since the wind stress varies with the area of impact. Additionally, the surface currents form large gyres in the subtropics and polar regions. There is a general consensus that the western boundary currents are comparatively faster and narrower than their eastern counterparts. These characteristics of the oceanic gyre are caused by western intensification, a phenomenon due to the Coriolis

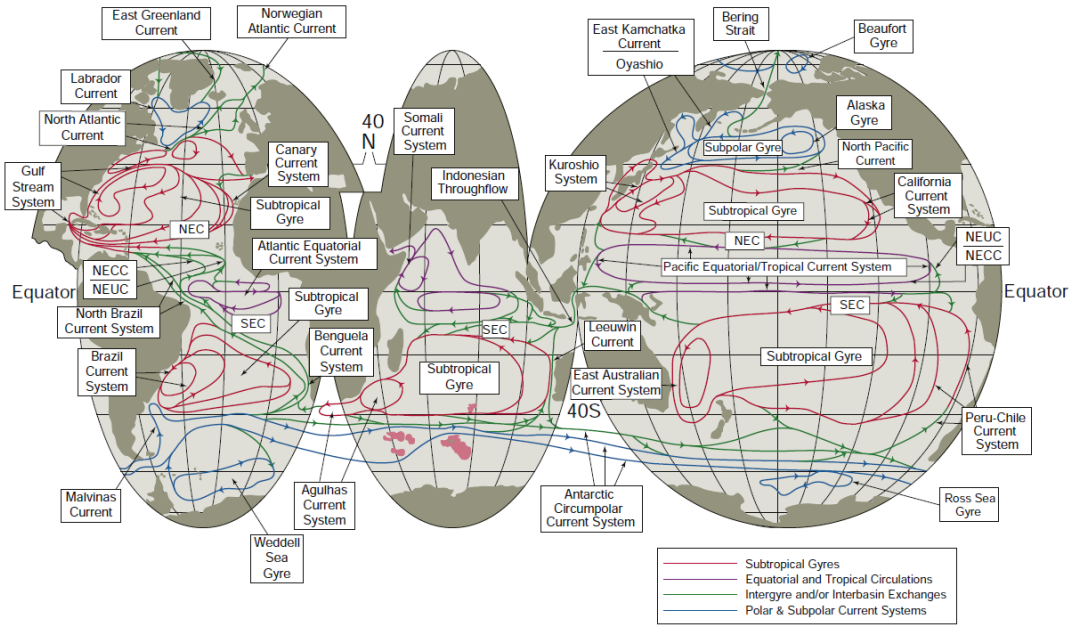

Figure 1.2: Schematic representation of surface currents in the global ocean. Reprinted from Talley et al. [2011], Schmitz [1996].

effect [Talley et al., 2011]. The eastern parts of subtropical gyres are relatively rich in nutrients and, these currents help maintain a relatively cold and dry climate over nearby continents. However, the biological productivity of the central subtropical gyres are very low due to strong stratification, and hence these regions are commonly referred to as oceanic desert. These gigantic subtropical gyres are responsible for transporting heat from tropical regions to high latitudes through the upper layers of the ocean. Often, the western part of these gyres act as a surface branch of thermohaline circulation. A recent study shows that the poleward shifting of gyres is likely happening as a consequence of global warming [Yang et al., 2020].

1.1.2 Thermohaline Circulation

The Thermohaline Circulation is also referred to as the meridional overturning circulation (MOC) or the global oceanic conveyor belt. The global MOC is a three-dimensional ocean circulation with pathways around the globe as shown in Figure 1.3.

An important process in the origin of MOC is the formation of deep water, for which near-surface water must be sufficiently dense. For really cold water at very high latitudes, the density variations of seawater are dominantly influenced by variations in salinity, whereas in the tropics, temperature changes become the dominant influence on

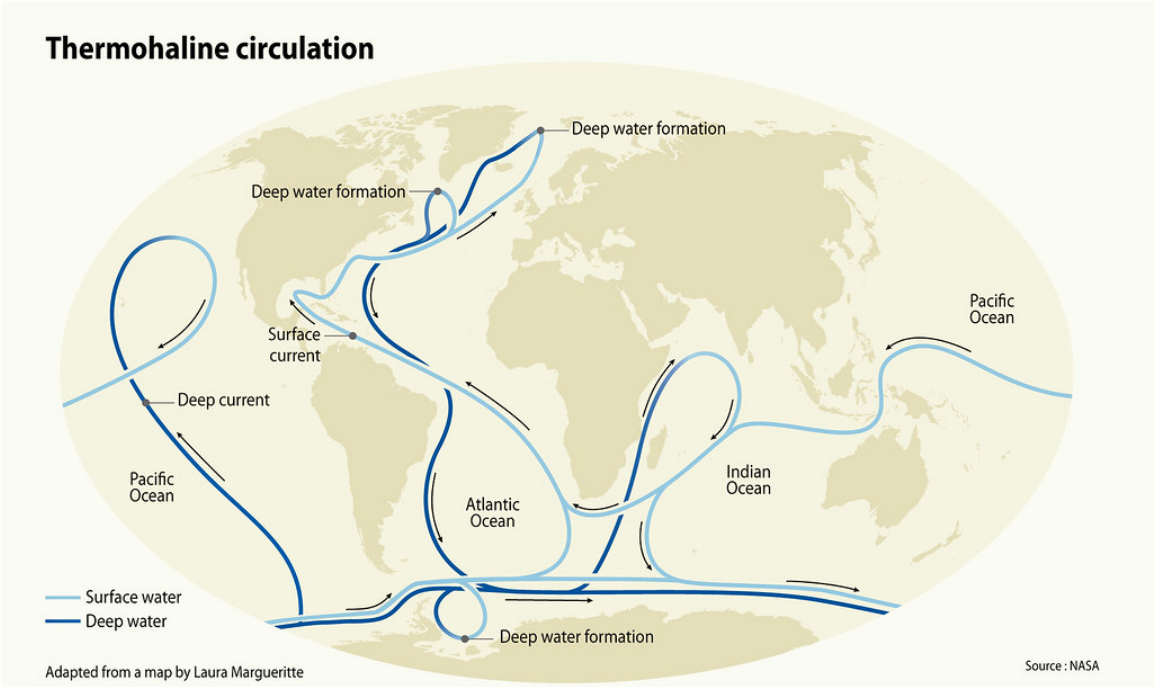

Figure 1.3: The pathways of global overturning circulation in the ocean. The light blue line represents the surface branch and the dark blue line represents the deep circulation. Reprinted from: GRID-Arendal website.

density variations. Therefore, deep water can only be formed in high latitudes, where near-surface temperature of the high saline water becomes sufficiently cold. The North Atlantic Ocean is one such region where the deep water masses form called the North Atlantic Deep Water (NADW). After downwelling, newly formed NADW moves southward and extends to deeper parts of global ocean. Munk and Wunsch [1998] estimated a global upwelling rate of 10^{-7} m s^{-1} from the equatorial Pacific Ocean, which is consistent with a recent estimate [Ganachaud and Wunsch, 2000]. Since the deep water movements are comparatively slower than that of the surface layers, the average time of deep water replenishment extends to several years. According to Gebbie [2012], the age of upwelled water is estimated to be around 1000 years, which is calculated by means of radiocarbon measurements in the Pacific Ocean.

In general, the MOC plays a key role (a) in maintaining the energy balance of Earth's climate and (b) in distributing heat and mass latitudinally. At very high latitudes, the radiative balance of the atmosphere varies due to seasonal changes in the amount of solar radiation. In winter time, the formation of sea ice keeps the subsurface water relatively warm and hence habitable to aquatic life. Due to its high albedo, sea ice can reflect more

than 70% of the incoming shortwave radiation. This keeps the polar climate colder than the tropics. However, the deficiency of absorbed shortwave radiation in the polar regions is partially balanced by heat transported from the tropics. The accumulated heat in the

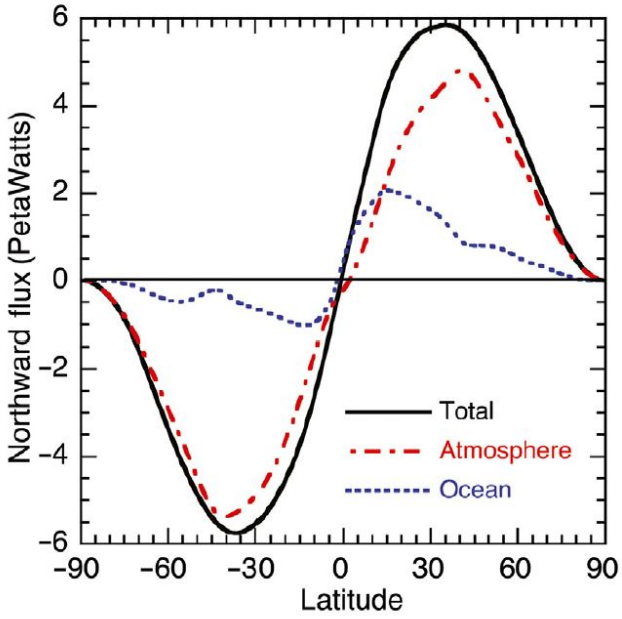

Figure 1.4: The annual mean meridional heat transport in petawatts (10^{15}W) by atmosphere and ocean. Reprinted from Hartmann [2015].

tropics is transported to the mid latitudes and polar regions through both atmospheric cells and ocean currents. Figure 1.4 compares the annual mean meridional heat flux carried across the latitudes by atmospheric and oceanic processes. This figure shows that the meridional heat transport (MHT) is dominated by the oceanic component in the tropics between 5° S and 15° N. On interannual timescales, the variability of the global oceanic MHT is dominated by the variations in the Indo-Pacific Oceans [Held, 2001, Trenberth and Caron, 2001, Hartmann, 2015, Ganachaud and Wunsch, 2000, Tandon et al., 2020]. Furthermore, the these interannual variations in oceanic MHT are strongly inflenced by the MOC variations [Tandon et al., 2020].

1.2 Importance of the Indo-Pacific Oceans

The Pacific Ocean is the largest and deepest ocean in the world. The Pacific Ocean is characterized by numerous marginal seas, mostly along the West Pacific. The Bering Strait is the narrow passage that links North Pacific to the Arctic. On the south side, the Pacific

Ocean is connected to the Southern Ocean. The surface circulation in the Pacific is mostly wind-driven, and in the tropics, the current system is dominated by strong zonal flows and counter-current systems. As shown in Figure 1.2, the North Equatorial Current (NEC) flows westward between 8° N and 20°N and the South Equatorial Current (SEC) spreads over 3°N and 10°S. The SEC is one of the fastest permanent currents in the world [Talley et al., 2011]. The North Equatorial Counter Current (NECC) lies around 5°N while its southern counterpart lies below the SEC.

On the other hand, the Indian Ocean is geographically peculiar due to its small size compared to other basins. It sits south of 25° N, and hence is not connected to the Arctic. There are many marginal seas, gulfs and straits in the Indian Ocean. The two important marginal seas are the Arabian Sea and the Bay of Bengal (BoB), which have contrasting oceanographic properties. Due to the high evaporation rate, the Arabian Sea has high salinity compared to the BoB. A large volume of fresh water from rivers originating from the Himalayas drains into the BoB. The BoB is relatively warmer than the Arabian Sea and is home to frequent tropical cyclones. The surface circulation patterns in the Indian Ocean are depicted in Figure 1.2, and it is characterized by seasonally reversing currents with a monsoonal wind system. The Indian Ocean is connected to the Southern ocean and thereby to the South Atlantic in the southwest through the Agulhas current. The Indian Ocean links to the South Pacific in the southeast through the west Australian current (also known as Leeuwin current). At low latitudes, the Indonesian Through Flow (ITF) links the Indian and the Pacific Ocean, transporting around 16 ± 3 Sv between these oceans [Ganachaud and Wunsch, 2000]. This low salinity water is then transported to the western tropical region by the South Equatorial Current (SEC). The reversal of the surface currents influences the biological productivity and weather patterns in the nearby areas. The variability of the current systems largely depends on the warming and the wind variability over the tropical region, especially on interannual timescales.

The formation of watermasses and deep circulation in the Indo-Pacific Oceans are different than in the Atlantic ocean. During winter, dense water forms in the Northeastern Arabian sea and occupies the sub-surface layers (100 to 300 m). The Red Sea and the Persian Gulf watermasses fill the layers below 400 m up to 1000 m. There is no deep water formation in the Indo-Pacific, and Antarctic Bottom Water (AABW) and NADW occupy the intermediate and deeper layers of the ocean. The AABW forms in the Southern Ocean, and is fresher and denser than NADW. The northward extent (north of 5°S) of these deep waters is controlled by the Seychelles Mauritius ridge. It is also known that

the Indo-Pacific MOC (PMOC) is the major contributor of interannual variability in the global MOC [Tandon et al., 2020]. Despite this potential importance, there has been little previous research on overturning in the deep Indo- Pacific [IPCC, 2013], and there are much fewer observations of the deep Indo-Pacific Oceans compared to the deep Atlantic.

The relevance of the Indian and Pacific Oceans is that these oceans are home to several climatic processes on different timescales like the El Niño Southern Oscillation (ENSO), the Indian Ocean Dipole (IOD), and the Indian Summer Monsoon. ENSO is a ocean-atmosphere couple mode of variability on interannual scales involving SST anomalies in the easter equatorial Pacific Ocean. In general, due to the piling up of warm water, the western tropical Pacific is referred as the Pacific warm pool [Philander, 1983, Wyrtki, 1975]. Even though ENSO is concentrated in the tropical Pacific, as a coupled ocean-atmosphere process, it affects global weather patterns. More importantly, ENSO is associated with changes to the Walker circulation and Hadley cell which can cause extreme events like drought and floods in South America, Australia, and East Asia. In addition to this, the changes in surface circulation affect biological productivity along the South American coasts, which are normally regions of coastal upwelling. Similar to the Pacific, the Indian Ocean plays a vital role in the global climate, being the warmest of the oceans. The IOD is a major ocean-atmosphere coupled mode of variability in the Indian Ocean similar to ENSO [Saji et al., 1999, Webster et al., 1999] and is partially linked to ENSO events. The IOD leads to severe drought and extensive precipitation over the Asian and African continent and Australia. The complexity of the Indian Summer Monsoon and the warming trend in the tropical Indian ocean makes it an important area of active research. The variability in the tropical Indo-Pacific Oceans associated with ENSO is potentially related to PMOC variability [Tandon et al., 2020]. However, the dynamical relationship between ENSO and PMOC remains unclear. Understanding of the mechanism of PMOC variability can advance the scientific knowledge of the dynamics of ENSO and other large-scale processes, and thereby help improve the climate models and climate prediction systems. This study attempts to elucidate the mechanism that drives PMOC variability.

1.3 Organization of Thesis

Chapter two provides more in-depth background on theories of the MOC, including the important scientific concepts, statistical techniques and analytic methods. This includes calculation of the MOC streamfunction, factors influencing MOC variability, and principal

component analysis. Chapter three describes the data and methods used for this study. In chapter four, the results and key pieces of the mechanism of PMOC variability are detailed. Chapter five summarizes the key results, conclusions, and future directions.

Chapter 2

PRELIMINARIES

This chapter describes the theoretical concepts relevant to the MOC. In particular, we explain the calculation of the MOC streamfunction, factors influencing MOC variability, and principal component analysis. We also discuss earlier studies related to the MOC in order to highlight the gaps that will be addressed in this study.

2.1 MOC Streamfunction

The study of the MOC is facilitated by representing motions in the latitude-depth plane using a single function. Hence, we use the MOC streamfunction Ψ which is a function of latitude and depth. The streamfunction represents the zonal average of the flow and shows where the meridional and vertical flows are important [Stewart, 2008].

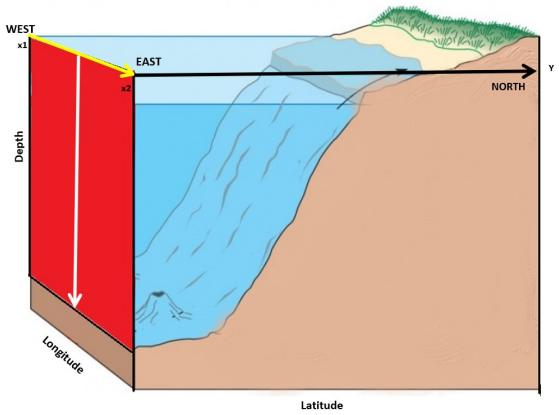

Figure 2.1: An illustration that represents the limits of integration for calculating MOC streamfuntion (Eq. 2.1). The yellow, black and white lines indicate longitude, latitude and depth axes respectively. The shaded area (red) indicates the longitude-depth plane where integration is performed to calculate MOC streamfuntion.

Let us consider the MOC streamfunction $\Psi\ (y, z, t)$ which is a function of y (latitude), z (depth, with $z = 0$ at a reference height for the ocean surface and positive values below that level) and t (time) that can be explicitly written in units of volume and is defined as:

$$\Psi(y, z, t) = -\frac{1}{\rho_0} \int_{x_1}^{x_2} \int_{z}^{H} \rho(x, y, z', t) v(x, y, z', t)\ dx dz'. \tag{2.1}$$

where ρ is the density of water; ρ_0 is a constant reference density of water; v is the meridional velocity in the ocean, x is longitude, and z' is the dummy depth. The function is integrated over the cross-sectional area of the relevant basin in the x–z plane below depth z, where the integration is performed in the positive x and z directions. The limits x_1 and x_2 represent the western and eastern boundaries of the relevant basin (explained later in section 3.2), and $H(x, y)$ is the ocean bottom at point (x, y) (See Figure 2.1). The cross-sectional area (x-z plane) of basin varies with latitude and topography, and the limits of integration also changes according to space when performing the streamfunction integral. The equation 2.1 can also be calculated using vertical velocity w. However, w is very small compared to horizontal velocities u and v, and is a derived quantity rather than a observed quantity. Hence, it makes easier to use meridional velocity v in equation 2.1.

For a basin with flat bottom topography, $v = 0$ at bottom. Positive values of Ψ indicate clockwise motion and negative values indicate counterclockwise when viewed from the east [Tandon et al., 2020]. In Boussinesq approximation, the contribution of density variations to the mass continuity equation becomes negligible and hence equation 2.1 reduces to:

$$\Psi(y, z, t) = -\int_{x_1}^{x_2} \int_{z}^{H} v(x, y, z', t) dx dz'. \tag{2.2}$$

The annual mean MOC streamfunctions for the global, Indo-Pacific and Atlantic basins are shown in Figure 2.2. It can be seen that the time mean global MOC is characterized by shallow overturning cells in the tropics and abyssal overturning in the Indo-Pacific basin (Figure 2.2b). The Atlantic MOC (AMOC) occupies the upper part of mean global MOC, spanning most latitudes (Figure 2.2c). The Southern Ocean MOC is excluded from the calculations due to the fact that there is no specific distinction between MOC in the Indo-Pacific and the Atlantic basins in the Southern Ocean region (south of 35° S).

Calculation of the MOC streamfunction reduces the complexity of representing volume transport in the latitude-depth plane. Climate models like the Canadian Earth System Model version 2 (CanESM2) combine the Indian and Pacific Oceans together while computing the MOC streamfunction. The magnitude of the PMOC variability is insensitive to the inclusion or exclusion of the Indian Ocean. Therefore, for this study, we focus on the Indo-Pacific MOC streamfunction (which we refer to simply as "PMOC") in order to facilitate comparison between models and observations.

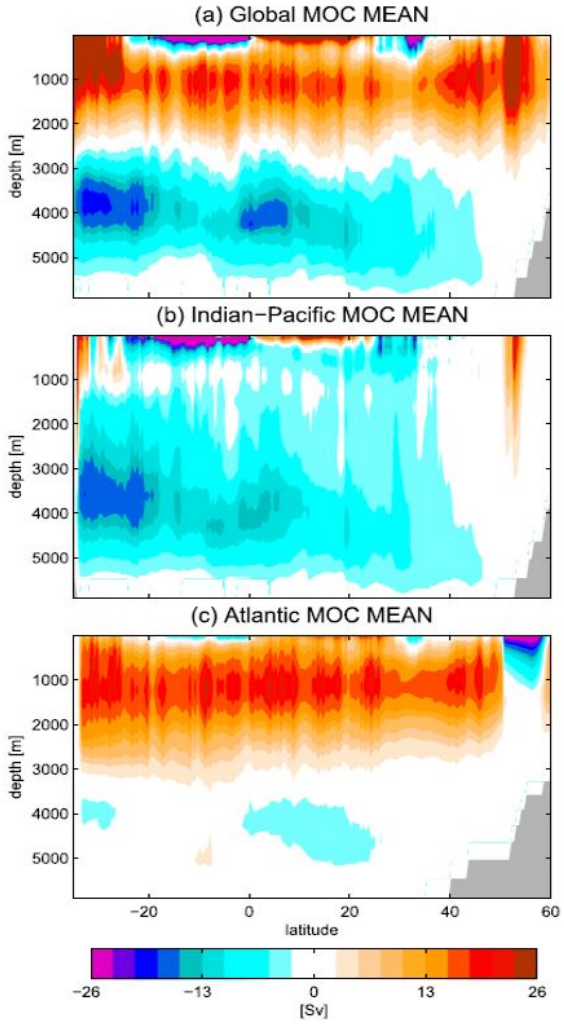

Figure 2.2: The annual mean MOC streamfunctions for the global, Indo-Pacific and Atlantic basins. Reprinted from Tandon et al. [2020].

2.2 Factors Influencing MOC Variability

The variability of the MOC can be driven by many physical factors depending on the timescale, basin, and location. The geological influences are considered fixed in time, and consist of topographical features such as ridges, trenches, and the continental slope. However, the tectonic movements alters the topographic properties, and underwater volcanic eruptions could result in changes to biological and chemical characteristics. The physical forcing includes sea-ice variations, fresh water input, wind stress and radiative flux input from the atmosphere. On interannual scales, the major forcings are 1) wind stress and 2) density variations.

2.2.1 Wind Stress and Ekman Transport

Wind stress is referred to as the horizontal force exerted by wind blowing above a fluid (in this case seawater) surface. When wind stress acts on the surface layers, it slightly moves the topmost layer of the ocean and generates momentum. This momentum is further transferred to deeper layers. Due to the planet's rotation, the momentum at the next layer down is deflected, and vanishes once it reaches the layer with zero momentum transfer. In other words, it is considered as the vertical transfer of horizontal momentum.

The variations happening in the upper layers of the ocean due to wind stress are explained by the Ekman theory developed in 1905 [Ekman, 1905]. Ekman theory is based on the assumption that the horizontal flow is steady and homogeneous while taking the effects of Earth's rotation into account [Stewart, 2008, Pond and Pickard, 1983]. Then, the horizontal and temporal derivatives are zero such that:

$$\frac{\partial}{\partial t} = \frac{\partial}{\partial x} = \frac{\partial}{\partial y} = 0. \tag{2.3}$$

For a flow on a rotating Earth, the above equation 2.3 results in the balance between frictional and Coriolis force. Assuming a constant vertical eddy viscosity,

$$\tau_{xz} = \rho A_z \frac{\partial u}{\partial z}, \qquad \tau_{yz} = \rho A_z \frac{\partial v}{\partial z}. \tag{2.4}$$

where τ_{xz}, τ_{yz} are the components of the wind stress in the x,y directions, A_z is eddy viscosity, ρ is the density of seawater, and u and v are velocities in x and y direction respectively. Here, the z axis is considered as positive in upward direction in accordance with the traditional approach to ocean Ekman layers.

The x and y momentum equations for a homogeneous, steady-state, turbulent layer are given by:

$$\rho f V + \frac{\partial \tau_{xz}}{\partial z} = 0 \qquad \rho f U - \frac{\partial \tau_{yz}}{\partial z} = 0. \tag{2.5}$$

where $f = 2\omega \sin\varphi$ is the Coriolis parameter for latitude φ, and ω is the angular velocity of Earth.

Using 2.4 in 2.5,

$$f v + A_z \frac{\partial^2 u}{\partial z^2} = 0 \qquad - f u + A_z \frac{\partial^2 v}{\partial z^2} = 0. \tag{2.6}$$

The boundary conditions are

$$\text{At } z = 0,\ A_z \frac{du}{dz} = \frac{\tau_x}{\rho_0} \text{ and } A_z \frac{dv}{dz} = \frac{\tau_y}{\rho_0}, \qquad \text{At } z = -\infty,\ u = v = 0. \tag{2.7}$$

The solution of the equation 2.6 can be written as

$$u = V_0\ \exp(az)\ \cos(\pi/4 + az) \qquad v = V_0\ \exp(az)\ \sin(\pi/4 + az). \tag{2.8}$$

for northward wind ($\tau = \tau_{yz}$) and the constants are:

$$V_0 = \frac{\tau}{\sqrt{\rho_w^2\ f\ A_z}},$$

and

$$a = \sqrt{\frac{f}{2A_z}}. \tag{2.9}$$

where V_0 is the velocity of sea surface current.
At the ocean surface, $z = 0$ and $\exp(z = 0)$, the solution 2.8 becomes,

$$u(0) = V_0 \cos(\pi/4), \qquad v(0) = V_0 \sin(\pi/4). \tag{2.10}$$

which means the direction of surface current will 45° to the right of wind direction in the Northern Hemisphere (NH) and it is 45° to the left of the wind direction in the Southern Hemisphere (SH). The magnitude of the current exponentially decreases with depth as per the equation 2.11. The net mass transport due to the Ekman currents will be 90° to the right of wind direction in the NH. This is schematically represented in Figure 2.3a.

$$\sqrt{u^2(z) + v^2(z)} = V_0 \exp(az) \tag{2.11}$$

Ekman theory is widely utilized to study upwelling in the ocean, especially, near coasts. The winds blowing along the coast can lead water to be displaced away from the shore. This results in the upwelling of cold subsurface water to replace the displaced surface water (see Figure 2.3b). The cold subsurface water is richer in nutrients, and this process leads to an increase in biological productivity in the upwelling region. The coasts of Peru and Somalia are examples of regions of coastal upwelling.

The temporal variability of wind stress acting on the sea surface can result in variations to Ekman transport. This will further lead to changes in horizontal and vertical

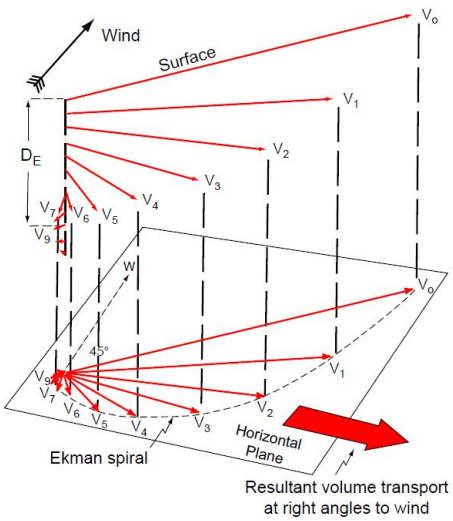

(a) Ekman Spiral

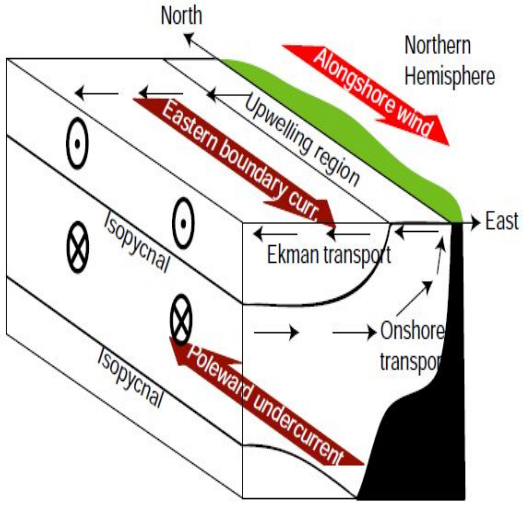

(b) Ekman transport and coastal upwelling

Figure 2.3: a) The schematic representation of velocities in the Ekman layer according to Eq. 2.11, and b) Coastal upwelling system due to an alongshore wind with Ekman transport away from the shore. The large arrow (red) in (a) indicates the direction of net transport. Reprinted from Talley et al. [2011].

transport. The divergence of horizontal velocities generates vertical motion, a process called Ekman pumping [Stewart, 2008]. The mathematical representation of the Ekman pumping is:

$$w_E = -curl_z\ (\frac{\boldsymbol{\tau}}{\rho f}). \tag{2.12}$$

where $\boldsymbol{\tau}$ is the wind stress vector and w_E is the Ekman Pumping.

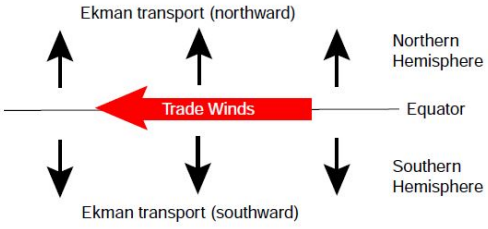

(a) Top view)

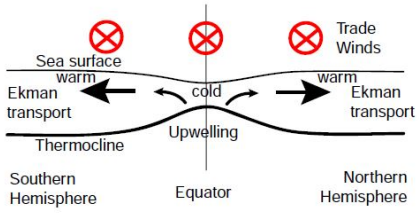

(b) Cross-sectional view

Figure 2.4: The schematic representations of divergence near equator due to the easterly trade winds and equatorial upwelling. Reprinted from Talley et al. [2011].

At the equator, Ekman theory is not valid as the Coriolis force becomes zero. Away from the equator (approx. 5° in both hemispheres), the easterly trade winds cause Ekman

transport to the north in the NH and south in the SH. This transport away from the equator leads to upwelling at the equator (see Figure 2.4a). This equatorial upwelling is supported by equatorward subsurface flow within the thermocline (Figure 2.4b). This equatorial undercurrent (EUC) is geostrophic, meaning that it is driven by the balance of Coriolis force and pressure gradient force. The pressure gradient force is generated due to the piling up of water which leads to high pressure in the western boundary relative to the east side. However, during an El Niño period, the anomalous tropical wind patterns leads to anomalous equatorial downwelling, and the surrounding warmer water replaces the downwelled water.

In the case of PMOC variability, the influence of wind stress on interannual timescales is already identified by Tandon et al. [2020], as will be explained later in section 2.4. In addition to driving Ekman transport, wind stress also plays a key role in generating buoyancy variations and the formation of deep water in the Antarctic and the North Atlantic Oceans (discussed earlier in section 1.1.2).

2.2.2 Density Variations

Seawater density is a function of temperature, salinity, and pressure (or depth). Potential density is often used to remove the effects of pressure on density, and isolate the portion of the density that can be used to generate irreversible motion. In general, the equation of state of seawater having salinity S and temperature T at a sea pressure p is expressed as

$$\rho(S,T,p) = \rho(S,T,0)/[1 - p/K(S,T,p)]. \tag{2.13}$$

where ρ is the density of seawater, K is the bulk modulus. For practical purposes, the equation of state is taken as a linear function ignoring the effects of pressure [Stewart, 2008, Pond and Pickard, 1983, Talley et al., 2003]. Then, the equation 2.13 will be modified as:

$$\rho \approx \rho_0 + \alpha(T - T_0) + \beta(S - S_0)\ , \qquad \text{where} \quad \alpha = \frac{\partial \rho}{\partial \mathrm{T}} \quad \text{and} \quad \beta = \frac{\partial \rho}{\partial \mathrm{S}}. \tag{2.14}$$

where ρ_0, T_0 and S_0 are arbitrary constant values of ρ, T and S, α is the thermal expansion coefficient (change in density for a given change in temperature) and β is the haline (saline) contraction coefficient (change in density for a given change in salinity). This equation (Eq. 2.14) is used to study the steric effects on density as will be discussed in the next chapter). Also, isopycnal (constant density) surfaces are often used as a vertical coordinate in the ocean,as horizontal motion is often along the surfaces of constant density. As in

the atmosphere, the vertical gradient of density determines the stability of the column and it has an impact on vertical mixing of the ocean. For practical purposes, the potential temperature and potential density are used. The potential temperature (θ) of a parcel in the ocean would have if it were moved adiabatically to a reference pressure (usually taken to be the pressure at the surface), and is expressed using a complex equation as defined in Fofonoff et al. [1905]. The potential density is the density of the parcel would acquire if adiabatically brought to a standard reference pressure, and can be calculated from equation 2.14 by replacing the temperature T with potential temperature θ. For convenience, the density of sea water is often expressed in terms of sigma-t (σ_t) and is given by

$$\sigma_t = \rho_t - 1000 \text{ kgm}^{-3}. \tag{2.15}$$

2.3 Principal Component Analysis (PCA)

Principal component analysis (also called Empirical Orthogonal Function (EOF) analysis) finds a set of independent functions, which can capture the structure of variability within a dataset. In oceanography, this analysis is useful to analyze the variability within a long timeseries of data. Edward Lorenz [Lorenz, 1956] developed a statistical EOF technique for weather prediction. A detailed history of PCA and EOF is described in Thompson and Emery [2014]. The advantage of EOF analysis is that, for a given timescale, it gives us a sense of the spatial structure of variability of data in terms of orthogonal functions (or "modes").

Following Ambaum [2004], consider an $m \times n$ data matrix, X, with n points in time and m in space. Then, the covariance matrix S is given by

$$S = \frac{1}{n-1} X^T X. \tag{2.16}$$

Each entry in matrix S contains the temporal covariance between two corresponding spatial points. Since $S^T = S$, the eigenvectors of S satisfy orthogonality. The eigenvalues and eigenvectors of S are,

$$S\psi^\alpha = \lambda_\alpha \psi^\alpha, \tag{2.17}$$

where α is the index of eigenvector ψ and eigenvalue λ. We can normalize each eigenvector as

$$|\psi^\alpha|^2 = \psi^\alpha \cdot \psi^\alpha = \lambda_\alpha. \tag{2.18}$$

By normalizing eigenvectors as in above equation 2.18, the eigenvectors can be represented with same units as that of standard deviation. Each eigenvector ψ^{α}has length m, corresponding to the number of spatial points. In PCA, the eigenvectors are referred as Empirical Orthogonal Functions (EOFs). Furthermore, any spatial pattern can be represented as a linear combinations of EOF matrices.

$$X_{ij} = \sum_{\alpha} p_i^{\alpha}(t) \cdot \psi_j^{\alpha}. \tag{2.19}$$

where i and j are the indices for time and spcae dimesions,respectively. The vector, $\boldsymbol{p^{\alpha}}$, denotes the principal component timeseries (PC) of the EOF, and it represents the amplitude of each EOF with respect to time. Each PC is obtained by projecting each EOF onto the original data using the relation

$$\psi^{\alpha} = \frac{1}{n-1}\, X^T p^{\alpha}. \tag{2.20}$$

The fraction of variance explained by a given mode α is given by $\lambda_{\alpha}/\sum_i \lambda_i$.

The spatial structure of the lowest mode represents the dominant mode of variability. That is, first mode will have the highest variance followed by subsequent modes with decreasing amplitude of variance. Even though EOF analysis imposes orthogonality constraints between modes which may affect the representation of non-dominant modes, we mainly focus on the first mode, which is not significantly affected by this orthogonality constraint [Richman, 1986]. Often only a couple of EOFs are needed to describe the variability. However, EOFs do not arise because of any physical mechanism, and establishing a physical mechanism for an EOF must be done through additional analysis or experimentation.

For analysis of PMOC variability, earlier studies have shown that the EOF analysis can be used effectively, especially, when the results need to be compared with output from climate models [Tandon et al., 2020]. Furthermore, the indices defined using a principal component time-series can be related other variables in order to investigate physical mechanism. More details are explained below in data and methodology (section 3.3).

2.4 Previous MOC studies

Most earlier studies focused on variability of the Atlantic and Southern Ocean MOC and their mechanisms [Talley et al., 2003, Keeling and Peng, 1995, Jackson et al., 2019]. However, the role of the Indo-Pacific MOC (PMOC) as a dominant driver of MHT variations

has recently been identified by Tandon et al. [2020]. Furthermore, the surface heat exchanges in the equatorial Pacific are linked with El Niño events [Izumo, 2005], and heat transport by the MOC dominates over the heat transport by the atmosphere near the equator [Held, 2001, Trenberth and Caron, 2001]. As discussed earlier, there is a strong relationship between MOC variations and ocean heat content. Variations in oceanic heat content can lead to deep ocean warming resulting in sea level variations [Lllovel et al., 2014].

Using Ocean General Circulation Model (OGCM), Jayne and Marotzke [2001] explained the variability of the PMOC on seasonal timescales. The seasonal variability of the PMOC is characterized by a single clockwise overturning cell spanning the tropics (Figure 2.5). The seasonal variability of PMOC is primarily driven by Ekman transport in the upper layers. Equatorially antisymmetric zonal wind stress are responsible for the northward Ekman transport. This transport generates depth independent flow in the deeper layers of the ocean and drives the overturning cells. Their experiment also indicated that free surface (or sea surface height) variations are associated with the flow in the upper layers. Furthermore, Jayne and Marotzke [2001] indicated that the seasonal variability of the PMOC also accounts for changes in meridional heat transport, and the amplitude of such variations are comparable to the atmospheric heat transport variations near the equator.

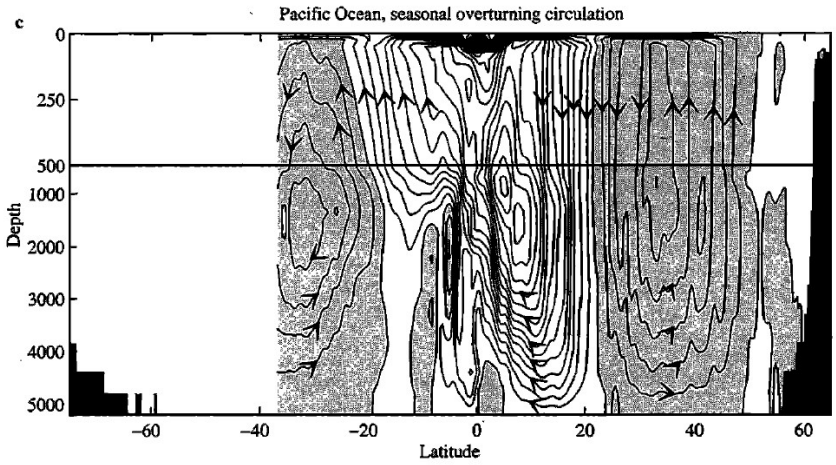

Figure 2.5: The seasonal (January minus July) MOC streamfunction in the Pacific . Negative values of the streamfunction are shaded, and contour interval is 2.5 Sv. Reprinted from Jayne and Marotzke [2001]

On interannual timescales, variability of PMOC is characterized by a deep cross-equatorial cell (CEC) spanning the full depth of the ocean in the tropics[Tandon et al., 2020]. Furthermore, controlled simulations indicated that wind stress variations are the

dominant driver of the CEC, and Tandon et al. [2020] showed that the variability in the PMOC accounts for almost all of the interannual standard deviation (ISTD) of the global MHT.

In constrast with seasonal variability, however, the zonal wind stress (ZWS) anomalies associated with the interannual variability of the PMOC are symmetric across the equator and positive within the region of the CEC. Therefore, the Ekman transport variations cannot explain the CEC using a mechanism identical to that used on seasonal timescales. Interannual variability of the PMOC is important to understand because of its potential role in climate variability and ENSO. Despite this potential importance, no one to the best of our knowledge has explained the mechanism of CEC. This study elucidates key pieces of the mechanism responsible the interannual PMOC variability.

2.5 Objectives and Hypotheses

The overall objective of this study is to understand the mechanism that drives the interannual variability of the PMOC. The specific research questions to be addressed are:

- What is the dominant structure of PMOC variability on interannual timescales?
- How does the wind stress influence the circulation cell associated with the variability of the PMOC?
- What is the role of Ekman transport in the near-surface circulation?
- If it is not wind stress, what drives the variability? How are SSH anomalies related to the PMOC variations?

Statistical analyses were carried out to answer these questions. We will show:

- The northward flow associated with PMOC variability is driven by differences in SSH between north and south sides of the equator.
- SSH variations are generated by density variations rather than wind stress variations.
- The density variations are driven by temperature variations.

Chapter 3

DATA AND METHODOLOGY

This chapter explains the data and specific methods used in this study to establish the mechanism behind interannual PMOC variability. This will include details about how the data are sorted according to ocean basin and the seperation of the saline and thermal components of density.

3.1 Estimating the Circulation and Climate of the Ocean (ECCO)

This study uses ECCO state estimate version 4, release 2 [Forget et al., 2015, 2016]. These data were considered retrospectively from 1992 to 2011 and are interpolated to a 0.5° horizontal grid with 50 vertical levels. The dataset is generated by an ocean model forced by atmospheric fields which are derived from ERA Interim reanalysis [Dee et al., 2011]. ECCO is also constrained to sea surface temperature (SST) observations from the National Oceanic and Atmospheric Administration [Reynolds et al., 2002], satellite altimetry [Scharroo et al., 2004], the global network of Argo floats [Argo, 2020], and other in-situ and satellite measurements. ECCO outputs all of the necessary fields required to represent the time evolution of the ocean. ECCO also assumes time-invariant eddy viscosity (A_z in 2.4).The ECCO estimate has been previously been used for studies of the MOC in the Atlantic and Pacific [e.g., Tandon et al., 2020, Jackson et al., 2019]. For this study, we study use the following variables with units in parentheses:

- ETAN : Free Surface Height Anomaly (m)
- EVELMASS : Eastward Mass-Weighted Component of Velocity (m s^{-1})
- NVELMASS : Northward Mass-Weighted Component of Velocity (m s^{-1})
- oceTAUE : Eastward Surface Wind Stress, τ_x (N m^{-2})
- oceTAUN : Northward Surface Wind Stress, τ_y (N m^{-2})
- RHOAnoma : Density Anomaly (kg m^{-3})
- SALT : Salinity (psu = g kg^{-1})

- THETA : Potential Temperature (°C)

3.2 Data Processing

The first step of the data processing was to separate the fields for the Indo-Pacific basin from the global data. For this purpose, a mask file was generated on the same grid as the ECCO data. For each ocean basin, a specific number is assigned as in Figure 3.1. Then data for each variable are filtered for the Indo-Pacific by requiring that the local mask value is equal to 2 or 3. Zonal mean values are determined by averaging from the eastern edge

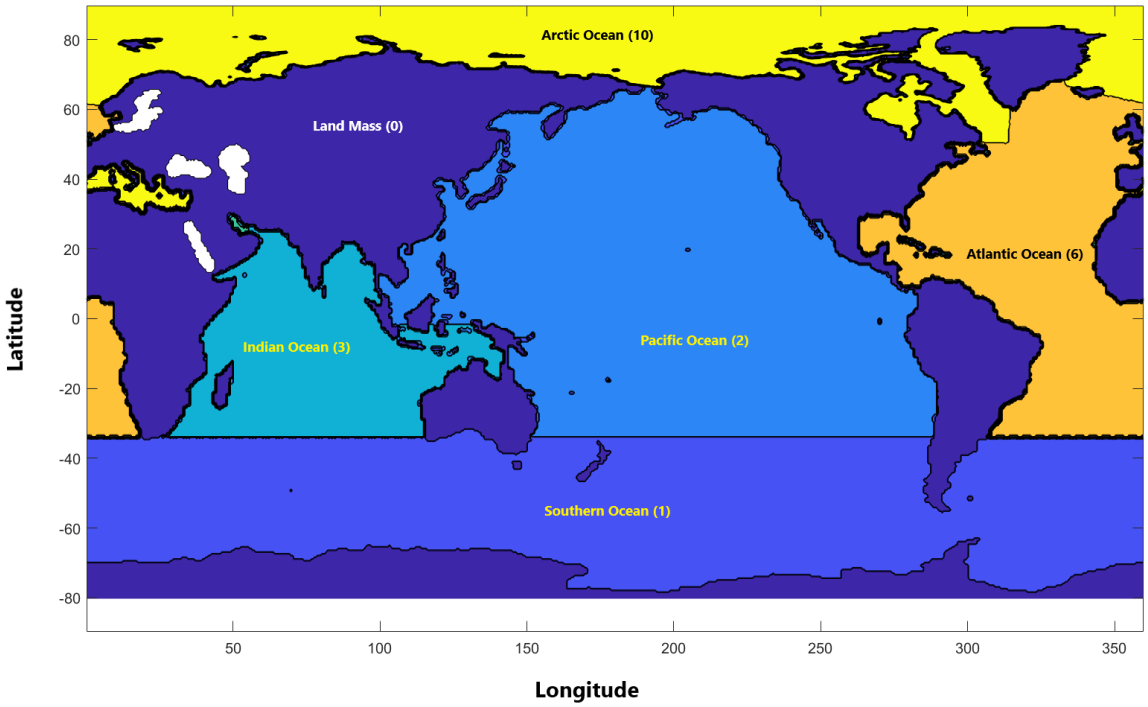

Figure 3.1: The mask file for filtering ECCO data according to each ocean basin. The basin identification numbers are shown in parentheses.

of the Pacific basin to the western edge of the Indian basin. The long-term linear trend is substracted from the data in order to mostly remove the effect of long-term climate change and focus on interannual variability. NaN values (corresponding to grid cells under land or below the ocean floor) are excluded from all calculations.

3.3 PMOC Variability and Dynamical Relationships

Following Tandon et al. [2020], interannual variability is quantified by calculating the Interannual Standard Deviation (ISTD). ISTD is the standard deviation of the annual mean.

The dominant mode of circulation is identified using an EOF analysis on the annual mean MOC streamfunction as described earlier (section 2.3 and 2.1). The principal component analysis of annual mean MOC streamfunction using ECCO is carried out on a data matrix with 18000 spatial points (m) and 20 points in time (n). The NaN values in the data matrix is replaced by zero while calculating the covariance matrix. The "PMOC index" is defined as the principal component timeseries of the first EOF over the domain $18°\text{S} - 20°\text{N}$ latitude below 500 m depth, and this index captures the behaviour of the CEC. Linear regression analysis is performed to see how PMOC index relates to other physical quantities.

3.3.1 Role of SSH in driving near-surface flow

We use SSH to find what drives the anomalous northward circulation at the surface of the ocean. The gradient of SSH can indicate the direction of the horizontal pressure gradient force (PGF) as well as sea level variations. In other words, the SSH is a combination of both dynamic height and steric height. The dynamic height (D) is a measure of the local force due to gravity and can be represented as

$$\Delta D = -\Delta\Phi = \int \delta \, dp/10. \tag{3.1}$$

where, Φ is the geopotential height (m^2s^{-2}), δ is the specific volume anomaly between two isobaric (constant pressure) surfaces with difference dp. The dynamic height is measured in units of dynamic metre, 1 dyn m = 10 m^2s^{-2}.

Steric height changes are produced due to both thermal and saline effects in the water column. If dynamic height is removed from the mean global sea level, the remainder is steric height, which is often used to depict the effect of global warming. The steric height anomaly, η', is defined by Gill and Niller [1973] as

$$\eta' = -\left(\frac{1}{\rho_0}\right)\int_0^H \rho' \, dz. \tag{3.2}$$

To evaluate the effects of salinity and temperature as mentioned in section 2.14, we

can express the density anomaly as,

$$\rho' = \rho_0 \left(-\alpha_T \, T' + \beta_S \, S'\right). \tag{3.3}$$

where T' and S' are anomalies of temperature and salinity and α_T and β_S are coefficients of thermal expansion and saline contraction, respectively. Thevalue of α_T ranges from 1×10^{-4} C^{-1} to 3×10^{-4} C^{-1}, and β_S ranges from 7×10^{-4} to 8×10^{-4} [Vivier et al., 2011]. The equation 3.2 becomes

$$\eta' = \int_0^H \alpha_T \, T' dz - \int_0^H \beta_S \, S' dz. \tag{3.4}$$

The coefficient values (α_T, β_S) are taken to be $\alpha_T = 2 \times 10^{-4}$ C^{-1} and $\beta_S = 7.5 \times 10^{-4}$, the average of typical values for the Pacific Ocean. To isolate the effect of temperature, S' in equation 3.4 is kept constant by substituting climatological mean values. Conversely, to isolate the effect of salinity, T' in equation 3.4 is substituted with climatological mean values.

Furthermore, the role of density variations in driving the pressure gradient flow can be established using the Kelvin circulation theorem, which relies on the following identity for a barotropic fluid:

$$\nabla\rho \times \nabla p = 0 \tag{3.5}$$

Considering only the k component of the above cross product,

$$\left(\frac{d\rho}{dx}\right)\left(\frac{dp}{dy}\right) - \left(\frac{dp}{dx}\right)\left(\frac{d\rho}{dy}\right) = 0. \tag{3.6}$$

$$\left(\frac{dp}{dy}\right) = \left(\frac{dp}{dx}\right)\left(\frac{d\rho}{dy}\right) \cdot \left(\frac{d\rho}{dx}\right)^{-1}. \tag{3.7}$$

By chain rule, $\left(\frac{dp}{dx}\right)\left(\frac{d\rho}{dx}\right)^{-1} = \left(\frac{dp}{d\rho}\right)$, and equation 3.7 can be written as

$$\left(\frac{dp}{dy}\right) = \left(\frac{dp}{d\rho}\right)\left(\frac{d\rho}{dy}\right). \tag{3.8}$$

Equation 3.8 implies that the merdional pressure gradients are driven by the gradients of density, which can be produced by gradients in temperature and/or salinity. This explanation also establishes the role of steric SSH in driving pressure gradient flow.

3.3.2 Role of ocean currents in driving temperature anomalies

The heat budget at a particular location of the ocean can expressed using a simple equation as

$$Q_T \;=\; Q_S + \; Q_b + \; Q_h + \; Q_e + \; Q_v. \tag{3.9}$$

where Q_T is the total rate of gain or loss of heat, Q_S is rate of heat gain due to shortwave radiation through the sea surface, Q_b is net heat loss by the sea as longwave radiation, Q_h is the rate of sensible of heat flux, Q_e is the rate of latent heat flux, and Q_v is the rate of advective heat flux due to the ocean currents [Talley et al., 2011]. To assess the role of horizontal temperature advection within the ocean surface layer (Q_v), all the other terms except Q_v on the right hand side of equation 3.9 is assumed to be invariant with time. In this study, we consider the surface temperature assumed to be the potential temperature (θ) at 5 m depth, which is a better representative of heat content variations compared to the SST. Therefore, we consider the temperature equation, including only a tendency term and a horizontal advection term.

$$\frac{\partial \theta}{\partial t} \; + \boldsymbol{v} \cdot \nabla \theta \;=\; 0. \tag{3.10}$$

or

$$\frac{\partial \theta}{\partial t} \; = -u \frac{\partial \theta}{\partial x} \; - v \frac{\partial \theta}{\partial y}. \tag{3.11}$$

where u and v are velocties in x and y directions, respectively. The equation 3.10 assumes the Boussinesq approximation, and hence the work term from the first law of thermodynamics reduces to $\frac{1}{\rho} dp$. Since the equation 3.11 uses potential temperature, the work term is negligibly small, and therefore is neglected.

Substituting the mean (bar) and deviation from the time mean (prime) of each variables such that $\theta = \bar{\theta} + \theta'$, $u = \bar{u} + u'$, and $v = \bar{v} + v'$, we obtain,

$$\frac{\partial \bar{\theta}}{\partial t} \; + \frac{\partial \theta'}{\partial t} \; = -\bar{u} \frac{\partial \bar{\theta}}{\partial x} \; - \bar{v} \frac{\partial \bar{\theta}}{\partial y} \; - \bar{u} \frac{\partial \theta'}{\partial x} \; - \bar{v} \frac{\partial \theta'}{\partial y} \; - u' \frac{\partial \bar{\theta}}{\partial x} \; - v' \frac{\partial \bar{\theta}}{\partial y} \; - u' \frac{\partial \theta'}{\partial x} \; - v' \frac{\partial \theta'}{\partial y} \; . \tag{3.12}$$

We assume $u' \frac{\partial \theta'}{\partial x}$, $v' \frac{\partial \theta'}{\partial y}$, $\bar{u} \frac{\partial \theta'}{\partial x}$, and $\bar{v} \frac{\partial \theta'}{\partial y}$ are negligibly small, and $\frac{\partial \bar{\theta}}{\partial t} \; = -\bar{u} \frac{\partial \bar{\theta}}{\partial x} \; - \bar{v} \frac{\partial \bar{\theta}}{\partial y}$, and we obtain the advection of temperature anomaly θ'_{adv},

$$\frac{\partial \theta'_{adv}}{\partial t} \; = -u' \frac{\partial \bar{\theta}}{\partial x} \; - v' \frac{\partial \bar{\theta}}{\partial y}. \tag{3.13}$$

We will test our above assumptions later by comparing the pattern of heating given by equation 3.13 with the actual temperature anomalies in the surface layer of the ocean.

Chapter 4

RESULTS AND DISCUSSION

This chapter includes the results from this study and discussion of the mechanistic chain that explains the CEC. The hypotheses are tested using statistical methods, and the roles of the variables that drive the CEC are described in detail.

4.1 Interannual Variability of PMOC

Firstly, the ISTD of the MOC streamfunction for the Indo-Pacific basin is shown in Figure 4.1. From Figure 4.1, it can be seen that the region of strongest variability is concentrated in the tropics. The variability of the PMOC in the equatorial region is nearly 4 Sv in the upper 500 m, which is much higher than in the high latitudes. In contrast with the time-mean PMOC (Fig. 2.2), which is mostly confined to the upper ocean, the variability of the PMOC spans the full depth of the ocean. The PMOC variability has a large-scale organized strcture, despite having no such specific structure in the time-mean PMOC.

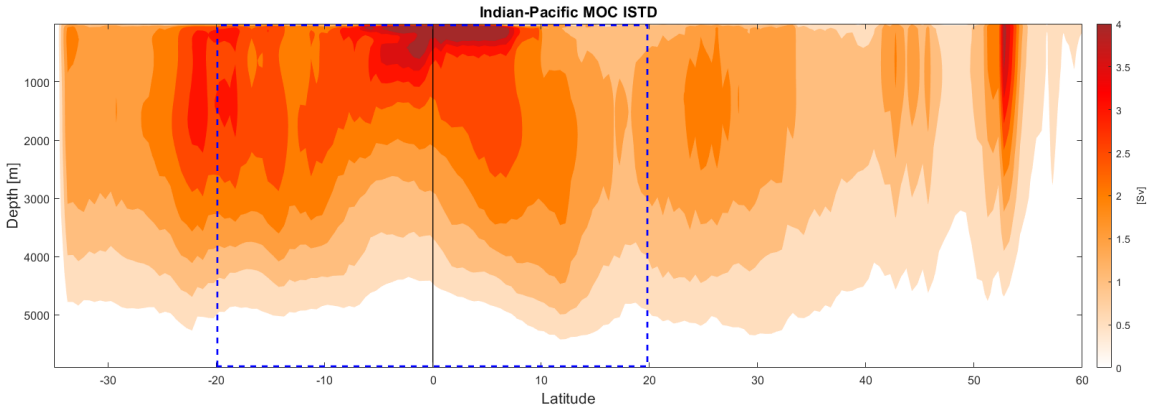

Figure 4.1: The interannual standard deviation of MOC streamfunction for the Indo-Pacific basins calculated from the ECCO state estimate. The region occupied by the CEC is marked by dashed box. The shading interval is 2.5 Sv.

To identify the dominant mode of the variance of the PMOC in the deep ocean (below 500m), a principal component analysis was carried out. We first performed PCA over the domain 35°S - 60°N (not shown). This analysis revealed several overturning cells confined

to different latitude bands and spanning the full depth of the ocean, including the CEC in the 18°S - 20°N region (dashed box in Figure 4.1), which is our current focus. The first EOF of the PMOC over the domain 18°S - 20°N is shown in Figure 4.2a, and it accounts for 51% of the total variability. The second EOF (Figure 4.2b) is characterized by a dipole anomaly that explains 27% of the variability [Tandon et al., 2020]. The first EOF represents the positive phase of CEC (i.e. postive first principal component, "PC1") dynamically implies a clockwise overturning cell with the upper layer flow moving northward. In the deeper part of the CEC between 2 km and 4 km, there is southward return flow. The CEC has a downwelling branch on the northern side, and an upwelling branch on the southern side. This CEC is also present in analysis with different datasets (not shown). Hence, this spatial structure can be considered as a robust dynamical representation of the leading mode of interannual PMOC variability in the tropics. The main objective of this study is to explain the mechanism of the CEC.

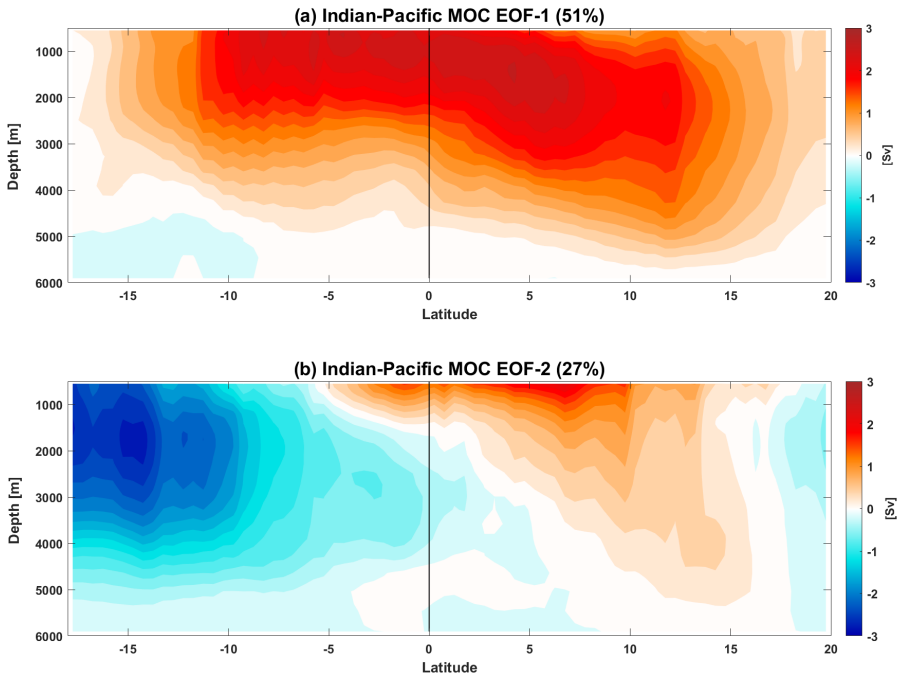

Figure 4.2: The (a) first and (b) second EOF of annual mean PMOC calculated from ECCO between 18° S and 20°N below 500m in the Indo-Pacific Ocean. Depths above 500m have been excluded to focus on variations in deep overturning rather than shallow overturning. The percentage of variance explained is indicated in parentheses above each panel, and the shading interval is 0.3 Sv.

The PC1 timeseries associated with the first EOF of the PMOC is shown in Figure 4.3. The time-series of PC1 captures the time variations of the CEC, and it can be used as

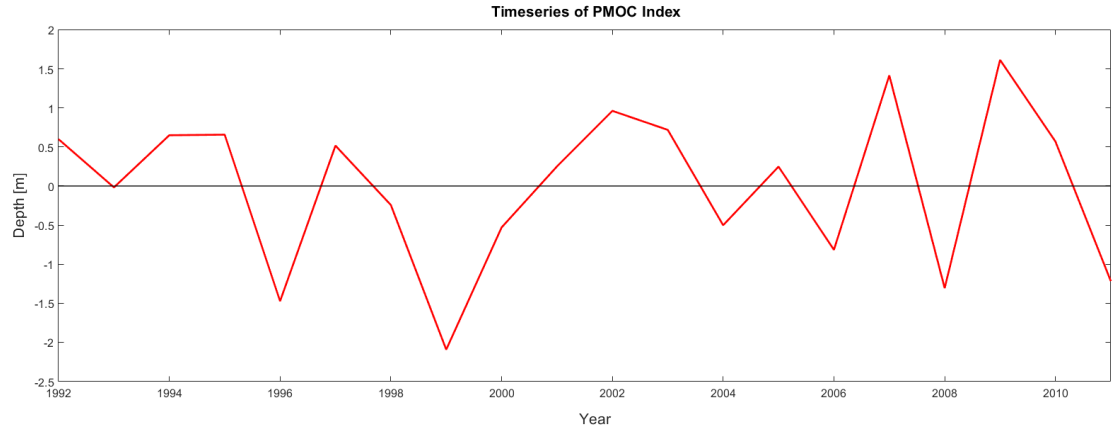

Figure 4.3: The first principal component timeseries corresponding to the first EOF shown in Figure 4.2.

an index to relate the CEC with other variables as explained in section 2.3. Positive values of PC1 indicate that the phase of EOF1 is positive, implying an anomalously clockwise CEC. Conversely, negative PC1 implies an anomalously counterclockwise CEC. Hereafter, we refer to PC1 as the "PMOC Index".

4.2 Mechanism Behind the CEC

As discussed earler, the mechanism behind the CEC has yet to be understood. This section presents additional analysis to elucidate the CEC mechanism.

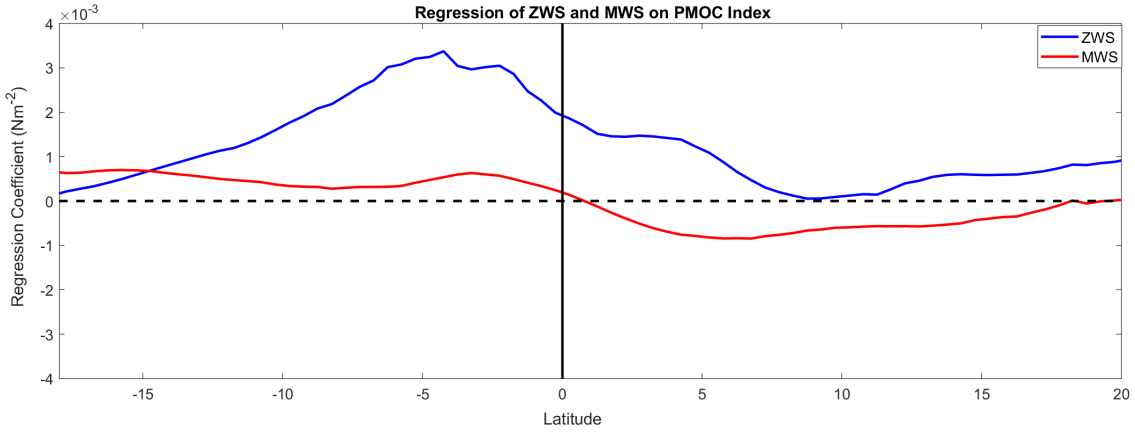

Figure 4.4: Regressions onto the PMOC index of annual mean zonally averaged wind stress in the Indo-Pacific. Blue and red lines indicate the zonal and meridional wind stresses, respectively.

We first consider the role of the zonal and meridional wind stresses. Figure 4.4 shows the linear regression onto the PMOC index of the annual mean zonal mean zonal (blue) and meridional (red) wind stress in the Indo-Pacific. In other words, Figure 4.4 shows what the wind stress anomalies typically look like when the PMOC index is positive (indicating northward transport across the equator in the upper Pacific Ocean). The ZWS is potentially important because it can drive Ekman transport in surface layers. The regression analysis reveals that the ZWS anomalies are eastward at most latitudes. This result reveals that ZWS-driven Ekman transport is not responsible for the northward surface flow in the postive phase of the CEC since positive ZWS would imply Ekman transport convergence near the equator.

Interestingly, the MWS anomalies are showing a similar sign to that of the climatological mean MWS. In other words, the MWS anomalies indicate a strengthening of the trade winds for which the meridional component is negative (southward) in the NH and positive (northward) in the SH. More importantly for our purposes, the MWS anomalies in the Figure 4.4 cannot explain the anomalous northward transport in the upper ocean associated with the positive phase of the PMOC index.

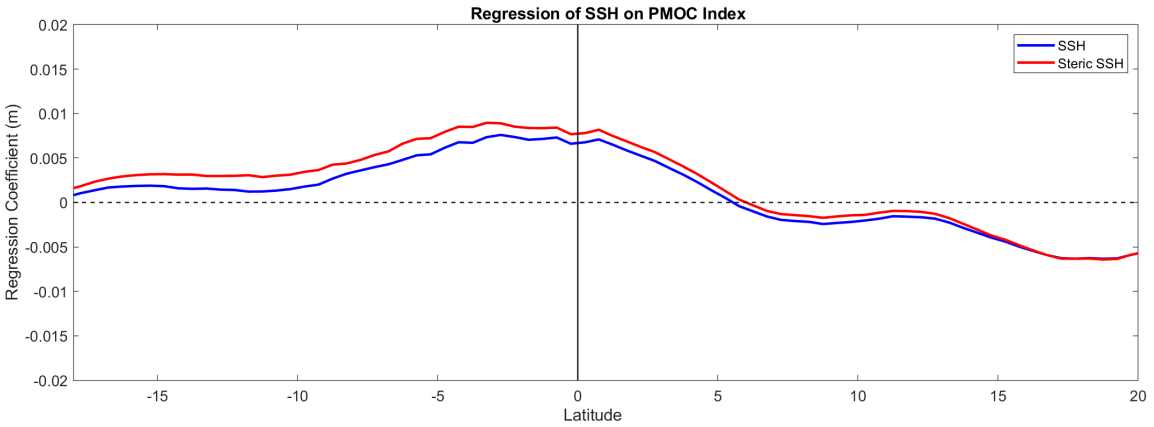

Figure 4.5: Regressions on to PMOC index of annual mean zonally averaged SSH (blue) and steric SSH (red) anomalies in the Indo-Pacific.

If anomalous Ekman transport does not explain the near-surface flow in the CEC, what is the explanation? Anomalies of SSH can provide an alternative explanation, as they can induce a pressure gradient force (see section 3.3). The regression of SSH anomalies onto the PMOC Index is shown in the blue line in Figure 4.5. This calculation reveals that there is a north-south gradient of SSH. That is, SSH is anomalously high south of the equator and anomalously low north of the equator. Associated with these SSH anomalies is an

anomalously northward pressure gradient, which would generate northward flow across the equator. Thus, anomalies of SSH provide a key piece of the mechanism responsible for the near-surface branch of the CEC.

Furthermore, the hypothesis of SSH driving the CEC is confirmed with the lag correlation of the "SSH Seesaw Index (SSI)", which is a measure of the meridional SSH gradient around the equator, as in Figure 4.6. The SSI is defined as the SSH anomaly averaged over $10-15°$S minus the SSH anomaly over $10-15°$N. The SSI is positively correlated with the PMOC Index when the SSI leads by one year, indicating that a positive meridional SSH gradient around the equator drives a northward transport in the upper Indo-Pacific Ocean. The magnitude of SSH anomalies associated with PMOC variability are on the order of a centimetre.

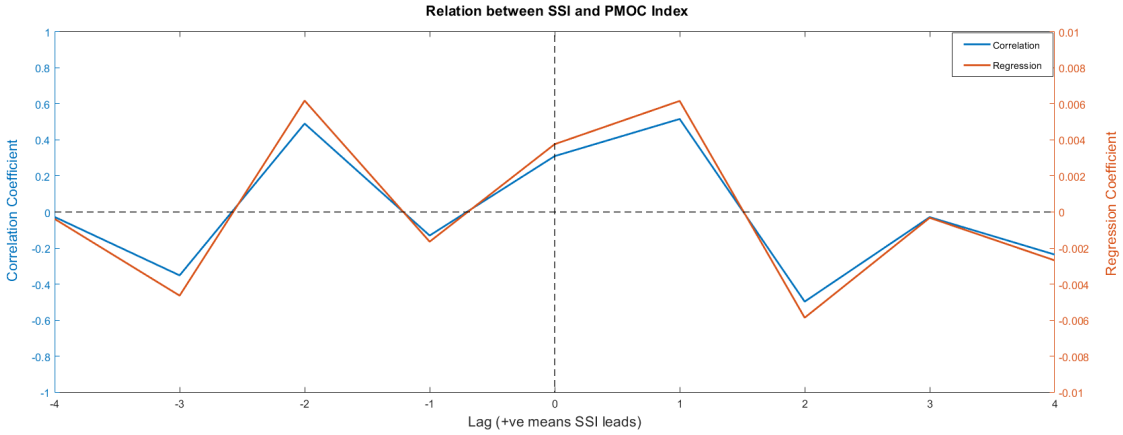

Figure 4.6: The lag correlation (blue) and lag regression(red) between the SSH Seesaw Index (SSI) and the PMOC Index. The positive values in the x axis indicate the SSI is leading the PMOC. See text for definition of SSI.

To what extent are the tropical SSH anomalies driven by density changes? To address this question, Figure 4.5, red line, shows the annual mean steric SSH anomalies in the Indo-Pacific regressed onto the PMOC index. Here, the steric SSH anomalies are computed using equation 3.2. From Figure 4.5, it can be seen that both the structure and magnitude of steric SSH anomalies closely follow the SSH variations. This result suggests that the SSH anomalies driving the CEC are indeed generated by density changes rather than dynamical changes.

Are these steric SSH anomalies generated primarily by temperature changes or salinity changes? To address this question, we have isolated the temperature and salinity contributions to the steric density anomalies (as described in section 3.3), and regressed each of

these quantities onto the PMOC Index (Figure 4.7). The thermal regression in Figure 4.7 (red line) closely resembles the regressions in Figure 4.5, whereas the saline regression in Figure 4.7 (blue line) is relative flat with respect to latitude. This result suggests that the SSH anomalies driving the near-surface branch of the CEC are generated by temperature anomalies in the upper ocean. The deeper layers will compensate this cross-equatorial flow with a clockwise overturning cell.

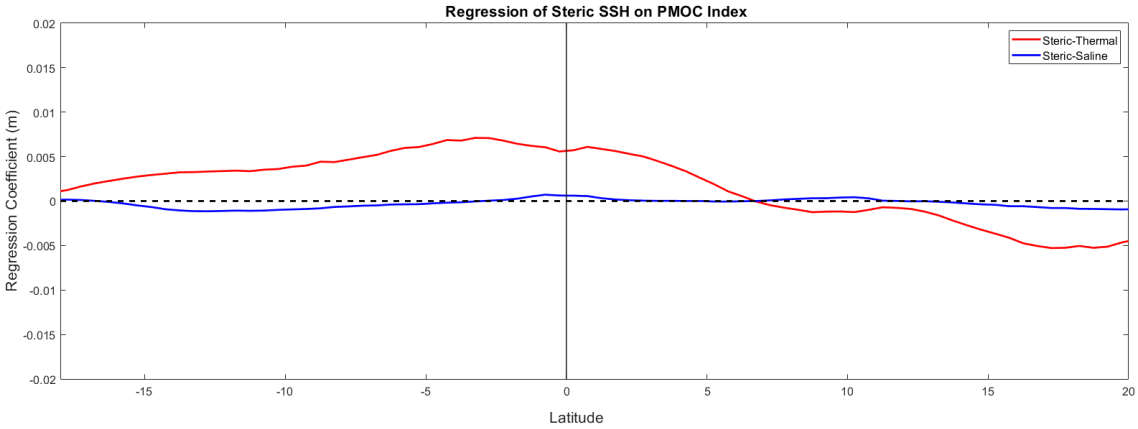

Figure 4.7: Regressions onto the PMOC index of annual mean zonally averaged thermal (red) and saline (blue) SSH anomalies in the Indo-Pacific.

4.3 Spatial Variability of SSH

To further understand how the temperature anomalies are generated in the tropics, we have produced regression maps (i.e. latitude-longitude plots of regression coefficients) of several quantities onto the PMOC index.

Figure 4.8 shows a regression map of SSH and steric SSH (contours) onto the PMOC Index. The spatial structure and magnitude of the total and thermal SSH anomalies are mostly the same. This builds on the results of Figures 4.7 and 4.5 to show that, throghout the Indo-Pacific basin, the SSH anomalies driving the CEC are thermally generated. Figure 4.8 shows that in the tropics, the SSH anomalies are postive in the Eastern Pacific and negative in the Western Pacific. At the equator, the positive SSH anomalies span approximately two-thirds of the basin width. Cool anomalies cover most of the subtropics and extratropics.

What is generating these temperature anomalies? The potential temperature at the top layer (5m) is a good indicator of heat content in the ocean surface layer. Figure 4.9 shows the regression onto the PMOC index of the potential temperature (θ) at 5m (shading)

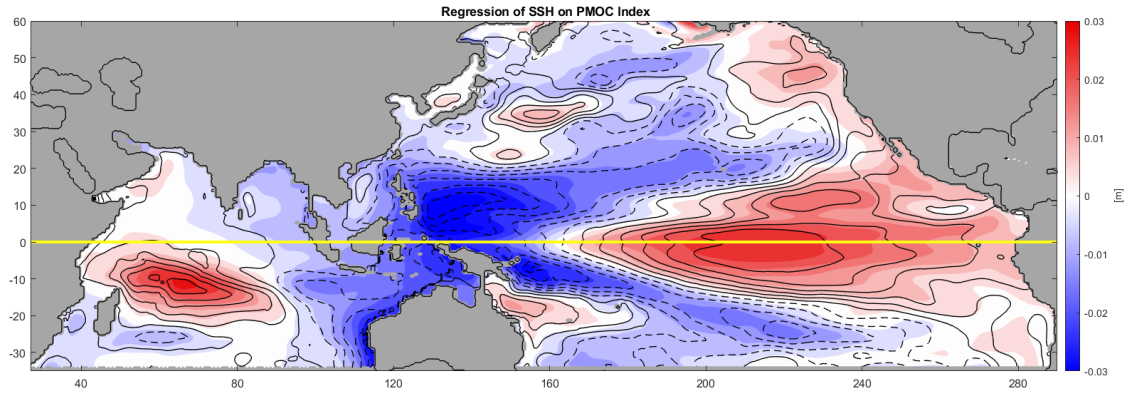

Figure 4.8: Map of the regression onto PMOC index of annual mean SSH (shading) and thermal SSH (contours) in the Indo-Pacific. The land masses and Atlantic Ocean are shaded with grey. The contour interval is 4×10^{-3} m.

and wind stress (vectors). Figure 4.9 shows that anomalies of wind stress are responsible for a strong eastward flow in the equatorial region, which would be expected to drive the warm water from the Western Pacific to the Eastern Pacific. The cool anomalies in the western and subtropical Pacific are associated with equatorward wind stress, suggesting that transport of cooler water or air from higher latitudes may be responsible for these anomalies.

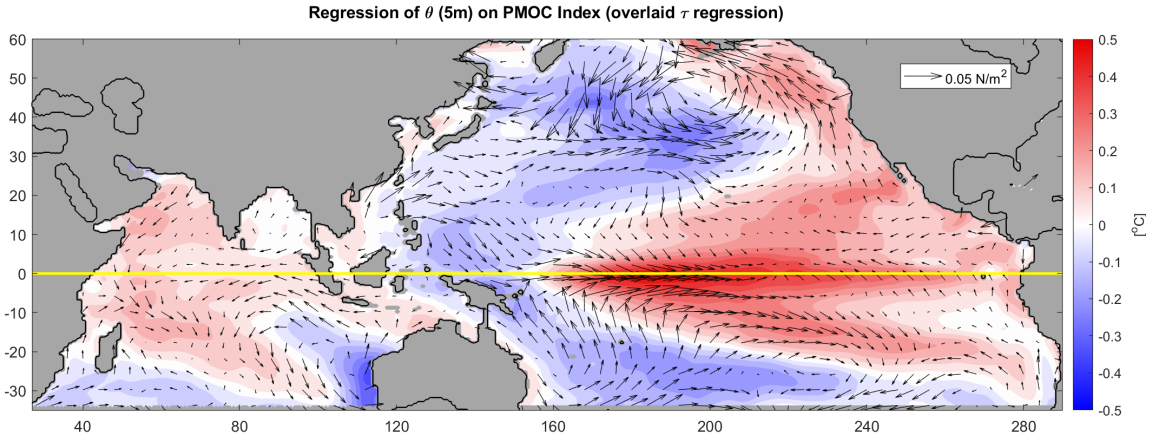

Figure 4.9: The regression onto the PMOC index of potential temperature (θ) at 5m (shading) and wind stress (vectors) in the Indo-Pacific. The shading interval is 0.05°C and the unit vector of wind stress represents magnitude of 0.05 N m^{-2}.

Are these temperature anomalies due to transport within the ocean or transport within the atmosphere? To further understand how the temperature anomalies are transported, the map of regression onto PMOC index of annual mean surface currents (vectors)

is produced (Figure 4.10), and it depicts how the anomalies of surface currents are associated with the PMOC variability. The regression patterns show a strong association between warm anomalies in the eastern equatorial Pacific and eastward transport in the ocean. This result suggests that wind-driven transport within the ocean may be responsible for generating warm anomalies in the eastern equatorial Pacific. Away from the equator, however, the role of the ocean currents appears to be small. We have also performed regressions of vertical velocity in the ocean onto the PMOC index, and these are also very small away from the equator. Altogether, these results suggest that atmospheric transport may play a primary role in generating the cooling anomalies in the subtropics. Furthermore, the spatial structure of the temperature changes is suggestive of changes driven by the atmospheric circulation, as similar anomalies driven by the atmospheric circulation are also apparent under El Niño [Sarachik and Cane, 2010].

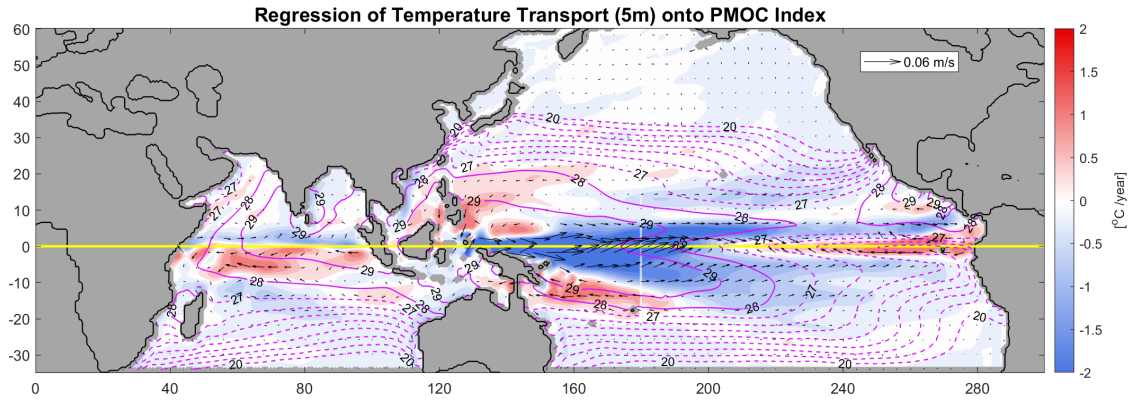

Figure 4.10: Map of the regression onto the PMOC index of annual mean temperature transport (shading), and ocean velocity at 5m (vectors) in the Indo-Pacific. Contour lines indicate climatological mean θ at 5m. The shading interval is 0.25°C per year, and contour interval is 1°C.

To further establish the role of surface currents, the ocean temperature horizontal advective heating anomalies ($d\theta'_{adv}/dt$) are calculated using equation 3.13. Figure 4.10 shows the regression of the annual mean $d\theta'_{adv}/dt$ (shading) onto the PMOC index, and the contours represent climatological mean potential temperature at 5m depth. Climatologically, the Western Pacific is warmer than the Eastern Pacific. The anomalous eastward flow at the equator would be expected to transport the relatively warm water from the Western Pacific to the Eastern Pacific, thus generating cool anomalies in the Western Pacific and warm anomalies in the Eastern Pacific, as is apparent in Figure 4.10. However, the spatial structure of $d\theta'_{adv}/dt$ is quite different from the temperature anomalies shown in Figure

4.9, and including vertical advection or additional horizontal advection terms in equation 3.13 does not improve the agreement. Altogether, these findings suggest that atmospheric transport plays a crucial role in determining the precise pattern of tropical heating and cooling, and transport within the ocean is not solely responsible for this pattern.

Chapter 5

CONCLUSIONS

In this study, the mechanism of the CEC is explained using a dynamic relation to SSH fluctuations in the upper layers of the Pacific Ocean. The simplified mechanism for the positive phase of the CEC is outlined as follows:

(a) On interannual timescales, around the equator, equatorward wind stress anomalies in the subtropics combined with anomalous eastward wind stress near the equator drive transport of warmer anomalies from the Western Pacific to the Eastern Pacific.

(b) The temperature anomalies in turn generate equatorially antisymmetric anomalies of zonal mean SSH. These SSH anomalies generate a pressure gradient from the south of the equator to the north of the equator.

(c) The pressure gradient drives northward cross-equatorial flow in the upper Pacific Ocean (above approximately 500 m).

(d) The anomalous cross-equatorial flow in the upper Pacific is compensated by a flow of water in the deep Pacific, thereby forming a clockwise overturning circulation cell.

Furthermore, this study relies on a single dataset, and hence we are verifying the results with additional datasets, including latest version of ECCO (release 4 version 4) as well as the Simple Ocean Data Assimilation (SODA) version 3.12.2. Even though PMOC variability is insensitive to the inclusion or exclusion of the Indian ocean, it is important to study the variability of Indian Ocean MOC, independently. The analysis of PMOC variability in different regions such as Western Pacific and Eastern Pacific is also an area for future research.

Interestingly, the SSH anomalies and the variations in potential temperature at 5m depth show a resemblance to temperature anomalies during El Niño. Tandon et al. [2020] performed analysis suggesting possible coupling between ENSO and PMOC. An in-depth understanding of this coupling may lead to better climate projections on interannual timescales, and this would be an important area for future research. Indeed, such improvement in ENSO prediction would be highly valuable, as it would allow governments to prepare for potentially devastating floods or droughts.

REFERENCES

Argo. (2020). *Argo float data and metadata from Global Data Assembly Centre (Argo GDAC)*. SEANOE. doi: https://doi.org/10.17882/42182.

Ambaum,Maarten H.P.,(2004). Lecture notes on "Calculating EOFs and principal component time-series", http://www.met.rdg.ac.uk/~sws97mha/Eofs/eof.pdf.

Davis, R. E. (1978). Predictability of sea level pressure anomalies over the North Pacific Ocean. Journal of Physical Oceanography, 8(2), 233-246.

Dee, D. P., Uppala, S. M., Simmons, A. J., Berrisford, P., Poli, P., Kobayashi, S., ... & Bechtold, P. (2011). The ERA-Interim reanalysis: Configuration and performance of the data assimilation system. *Quarterly Journal of the Royal Meteorological society*, 137(656), 553-597. doi:https://doi.org/10.1002/qj.828.

Ekman, V. W. (1905). On the influence of the earth's rotation on ocean-currents.doi: https://jscholarship.library.jhu.edu/bitstream/handle/1774.2/33989/31151027498728.pdf.

Fofonoff, Nicholas P., Millard, & Robert C., (1983),Algorithms for computation of fundamental properties of seawater, doi:https://hdl.handle.net/1912/2470

Forget, G., Campin, J.-M., Heimbach, P., Hill, C. N., Ponte, R. M., & Wunsch, C. (2015). ECCO version 4: an integrated framework for non-linear inverse modeling and global ocean state estimation. *Geoscientific Model Development*, 8, 3071-3104. doi:https://doi.org/10.5194/gmd-8-3071-2015.

Forget, G., Campin, J.-M., Heimbach, P., Hill, C. N., Ponte, R. M., & Wunsch, C. (2016). ECCO Version 4: Second Release. MIT Libraries DSpace@MIT. Retrieved from http://hdl.handle.net/1721.1/102062.

Ganachaud, A., Wunsch, C. (2000),Improved estimates of global ocean circulation, heat transport and mixing from hydrographic data. *Nature*, 408, 453–457. doi:https://doi.org/10.1038/35044048.

Gebbie, G. (2012), Tracer transport timescales and the observed Atlantic-Pacific lag in the timing of the Last Termination,*Paleoceanography*, 27, PA3225, doi: https://doi.org/10.1029/2011PA002273.

Gill, A. E. (1980). Some simple solutions for heat-induced tropical circulation.*Quarterly Journal of the Royal Meterological Society*. doi:https://doi.org/10.1002/qj.49710644905.

Gill, A., & Niller, P. (1973). The theory of the seasonal variability in the ocean. *Deep Sea Research and Oceanographic Abstracts*, 20(2), 141-177. doi:https://doi.org/10.1016/0011-7471(73)90049-1.

Hartmann, D. L. (2015). Global Physical Climatology (Vol. 103). *Newnes*.

Held, I. (2001). The Partitioning of the Poleward Energy Transport between the Tropical Ocean and Atmosphere. *Journal of Atmospheric Sciences*, 58, 943–948. doi:https://doi.org/10.1175/1520-0469(2001)058<0943:TPOTPE>2.0.CO;2

IPCC, 2013: Climate Change 2013: The Physical Science Basis. Contribution of Working Group I to the Fifth Assessment Report of the Intergovernmental Panel on Climate Change [Stocker, T.F., D. Qin, G.-K. Plattner, M. Tignor, S.K. Allen, J. Boschung, A. Nauels, Y. Xia, V. Bex and P.M. Midgley (eds.)]. *Cambridge University Press, Cambridge, United Kingdom and New York, NY, USA*, 1535 pp

Izumo, T. (2005). The equatorial undercurrent, meridional overturning circulation, and their roles in mass and heat exchanges during El Niño events in the tropical Pacific ocean. *Ocean Dynamics*, 55(2), 110–123. doi:https://doi.org/10.1007/s10236-005-0115-1

Jackson, L. C., Dubois, C., Forget, G., Haines, K., Harrison, M., Iovino, D., et al. (2019). The mean state and variability of the North Atlantic circulation: A perspective from ocean reanalyses. *Journal of Geophysical Research: Oceans*, 124, 9141– 9170. https://doi.org/10.1029/2019JC015210

Jayne, S. R., & Marotzke, J. (2001). The dynamics of ocean heat transport variability. *Reviews of Geophysics*, 39(3), 385–411. doi:https://doi.org/10.1029/2000RG000084

Keeling, R. F., & Peng, T.-H. (1995). Transport of heat, CO2 and O2 by the Atlantic's thermohaline circulation (Vol. 348). *Royal Society of London Philosophical Transactions Series B*. doi:https://10.1098/rstb.1995.0055

Lorenz, E. N. (1956). Empirical orthogonal functions and statistical weather prediction. URL:http://muenchow.cms.udel.edu/classes/MAST811/Lorenz1956.pdf

Llovel, W., Willis, J. K., Landerer, F. W., & Fukumori, I. (2014). Deep-ocean contribution to sea level and energy budget not detectable over the past decade. *Nature Climate Change*, 4, 1301-1035. doi:https://doi.org/10.1038/nclimate2387

Munk, W., & Wunsch, C. (1998). Abyssal recipes II: Energetics of tidal and wind mixing. Deep-sea research. Part I, *Oceanographic research papers*, 45(12), 1977-2010. https://www.whoi.edu/cms/files/Munk_Wunsch_DSR_1998_32129.pdf

Philander, S. G. H. (1983). El-Niño southern oscillation phenomena. *Nature*, 302(5906), 295-301. doi:https://doi.org/10.1038/302295a0

Pond, S., & Pickard, G. L. (1983). Introductory dynamical oceanography. *Gulf Professional Publishing*.

Richman, M.B. (1986), Rotation of principal components. J. Climatol., 6: 293-335. doi: https://doi.org/10.1002/joc.3370060305

Reynolds, R. W., Rayner, N. A., Smith, T. M., Stokes, D. C., & Wang, W. (2002). An improved in situ and satellite SST analysis for climate. *Journal of Climate*, 15(13), 1609–1625. doi:https://doi.org/10.1175/1520-0442(2002)015<1609:AIISAS>2.0.CO;2

Saji, N., Goswami, B., & Vinayachandran, P. (1999). A dipole mode in the tropical Indian Ocean.*Nature*, 401, 360–363 (1999). doi: https://doi.org/10.1038/43854

Sarachik, E. S.,& Cane, M. A. (2010). The El Niño-southern oscillation phenomenon. *Cambridge University Press*. doi: https://doi.org/10.1017/CBO9780511817496

Siedler, G., Gould, J., & Church, J. A. (2001). Ocean circulation and climate: observing and modelling the global ocean. *Elsevier*.

Scharroo, R., Lillibridge, J. L., Smith, W. H., & Schrama, E. J. (2004). Cross-Calibration and Long-Term Monitoring of the Microwave Radiometers of ERS, TOPEX, GFO, Jason, and Envisat.*Marine Geodesy*, 27(1-2), 279-297. doi:https://10.1080/01490410490465265

Schmitz Jr, W. J. (1996). On the World Ocean Circulation: Volume 2 The Pacific and Indian Oceans/A Global Update (No. WHOI-96-08). *WOODS HOLE OCEANOGRAPHIC INSTITUTION MA*. doi: https://10.1575/1912/356

Stewart, Robert H. (2008). Introduction to physical oceanography. Robert H. Stewart. Available electronically from http://hdl.handle.net/1969.1/160216.

Talley, L. D., Reid, J. L., & Robbins, P. (2003). Data-based meridional overturning srteamfunctions for the global ocean. *Journal of Climate*, 16(19), 3213-3226. doi:https://doi.org/10.1175/1520-0442(2003)016<3213:DMOSFT>2.0.CO;2

Talley, L. D. (2011). Descriptive Physical Oceanography: An Introduction. *Academic press*. doi:https://doi.org/10.1016/B978-0-7506-4552-2.10001-0

Tandon, N., Saenko, O., Cane, M., & Kushner, P. J. (2020). Interannual Variability of the Global Meridional Overturning Circulation Dominated by Pacific Variability. *Journal of Physical Oceanography*, 50, 559-574. doi:https://doi.org/10.1175/JPO-D-19-0129.1

Thomson, R. E., & Emery, W. J. (2014). Data Analysis Methods in Physical Oceanography. *Newnes*.

Trenberth, K. E., & Caron, J. M. (2001). Estimates of Meridional Atmosphere and Ocean Heat Transports. *Journal of Climate*, 14(16), 3433–3443. doi:https://doi.org/10.1175/1520-0442(2001)014<3433:EOMAAO>2.0.CO;2

Vivier, F., Kelly, K. A., & Thompson, L. (1999). Contributions of wind forcing, waves, and surface heating to sea surface height observations in the Pacific Ocean.*Journal of Geophysical Research*, 104(C9), 20767-20788. doi:https://10.1029/1999JC900096.

Yang, H., Lohmann, G., Krebs-Kanzow, U., Ionita, M., Shi, X., Sidorenko, D., et al. (2020). Poleward shift of the major ocean gyres detected in a warming climate.*Geophysical Research Letters*, 47, e2019GL085868. doi: https://doi.org/10.1029/2019GL085868

Webster, P. J., Moore, A. M., Loschnigg, J. P., & Leben, R. R. (1999). Coupled ocean–atmosphere dynamics in the Indian Ocean during 1997–98. *Nature*, 401(6751), 356-360. doi:https://doi.org/10.1038/43848

Wyrtki, K. (1975). El Niño—the dynamic response of the equatorial Pacific Oceanto atmospheric forcing. *Journal of Physical Oceanography*, 5(4), 572-584. doi: https://doi.org/10.1175/1520-0485(1975)005%3C0572:ENTDRO%3E2.0.CO;2